



# Diagnostics and energetics of the topographic Rossby waves generated by a typhoon propagating over the ocean with a continental shelf slope

Wei Yang<sup>1</sup> · Toshiyuki Hibiya<sup>2</sup> · Yuki Tanaka<sup>2</sup> · Liang Zhao<sup>3</sup> · Hao Wei<sup>1</sup>

Received: 14 February 2019 / Revised: 12 June 2019 / Accepted: 16 June 2019 / Published online: 26 June 2019  
© The Oceanographic Society of Japan and Springer Nature Singapore Pte Ltd. 2019

## Abstract

The dynamics of the subinertial response when a typhoon propagates over the ocean with a sloping bottom topography is investigated by carrying out a set of idealized numerical experiments. At least two different topographic Rossby waves (TRWs) are identified at the same along-slope wavenumber and two different subinertial frequencies in the wavenumber–frequency spectra. The diagnostics of vorticity balance demonstrates that the bottom pressure torque plays an important role in both the generation and propagation of TRWs. Two sets of sensitivity experiments show that the spatial structure of the typhoon is a “decisive” parameter in determining the along-slope wavenumber as well as the corresponding frequencies; the along-slope wavenumber of a TRW is first determined as a response to the typhoon-induced perturbation, and the corresponding frequencies are then determined so as to satisfy the theoretical TRW dispersion relationship. The amplitude of TRWs, in contrast, are controlled by both the typhoon radius as well as the typhoon traveling speed. For typhoons with a large radius or slow traveling speed, the resulting TRWs can be comparable to or more energetic than the near-inertial waves. This indicates that the TRWs might play an important role in inducing the near-bottom mixing along the shelf slope by using energy supplied from typhoon winds.

**Keywords** Topographic Rossby waves · Typhoon radius · Typhoon traveling speed · Vorticity balance · Continental shelf slope · Bottom pressure torque

## 1 Introduction

Most previous studies of the oceanic responses to travelling typhoons have focused on the generation and propagation of near-inertial waves (NIWs) (e.g., Gill 1984; Niwa and Hibiya 1997; Tada et al. 2018), with little attention paid to subinertial waves. Recently, however, several observations have successfully captured the generation of subinertial waves in response to typhoon passages. A group of subinertial waves with a period of 2–5 days, for example,

was observed after a hurricane traveled over the northeastern Gulf of Mexico (Teague et al. 2007). Based on an oceanic observing system in the northern Arabian Sea, Wang et al. (2012) observed subinertial waves with a period of 12.7 days after the passage of tropical cyclone “Gonu”. Igeta et al. (2011) also observed strong subinertial motions together with near-inertial oscillations off the eastern coast of Japan after a typhoon passage.

Topographic Rossby waves (TRWs) are representative subinertial motions resulting from the conservation of potential vorticity. They are trapped near the topography and propagate with shallower (deeper) water on their right in the northern (southern) hemisphere (Gill 1982). The observational evidence of TRWs has been widely presented over continental shelf slopes (Thompson and Luyten 1976; Pickart 1995; Oey and Lee 2002; Jensen et al. 2013; Rivas 2017) and mid-ocean ridges (Miller et al. 1996; Wang et al. 2012).

The generation of TRWs requires that a fluid parcel is shoved in the cross-slope direction. The conservation of potential vorticity then makes the fluid gain cyclonic

✉ Wei Yang  
yangwouc@163.com

<sup>1</sup> School of Marine Science and Technology, Tianjin University, Tianjin, China

<sup>2</sup> Department of Earth and Planetary Science, Graduate School of Science, The University of Tokyo, Tokyo, Japan

<sup>3</sup> College of Marine and Environmental Sciences, Tianjin University of Science and Technology, TEDA, Tianjin, China

(anticyclonic) relative vorticity when it is shoved onto deeper (shallower) topography. Typhoons can be an effective way to shove the fluid parcel when they travel over the sloping ocean bottom.

By solving a two-dimensional eigenvalue problem, Wang and Mooers (1976) showed the theoretical cross-slope structure of subinertial TRWs in the continuously stratified ocean. It was found that the density stratification has an important effect on the TRW modal structure: the TRWs are bottom-trapped over the shelf slope when the local baroclinic radius of deformation is larger than the shelf width, suggesting the possibility that they can create an efficient energy pathway toward the deep ocean to induce strong mixing near the ocean bottom. This is quite different from the NIWs which cannot penetrate into the deep ocean due to their low vertical group velocities (Furuichi et al. 2008). Indeed, there is increasing evidence that the TRWs play a very important role in ocean mixing processes by concentrating their energy on the ocean bottom and dissipating it efficiently (Tanaka et al. 2010; Damerell et al. 2012).

However, there still remain some key questions regarding typhoon-generated TRWs: which term in the vorticity equation is responsible for the generation and propagation of TRWs, how do the properties and energetics of the generated TRWs depend on the typhoon parameters, and what controls the relative amplitudes of the TRWs with respect to the NIWs?

The western North Pacific Ocean is the most active tropical cyclone basin in the world's oceans (Emanuel 2005). In this study, we analyze the generation and propagation of TRWs when typhoons travel over the ocean with a sloping bottom topography. For this purpose, we carry out idealized numerical experiments in which a typhoon is assumed to propagate perpendicular to the isobaths of the ocean with simplified sloping bottom topography and a typical density stratification, both representative of the East China Sea (ECS). Section 2 describes the numerical setting. A standard case of numerical simulation is analyzed in Sect. 3. Section 4 includes the discussions of the vorticity balance, the sensitivity of TRW properties to typhoon parameters, and the relative amplitudes of the TRWs with respect to the NIWs. Conclusions are presented in Sect. 5.

## 2 Numerical setting

Numerical experiments were carried out using the Massachusetts Institute of Technology General Circulation Model which solves the free surface Boussinesq equations under the hydrostatic approximation. The model domain is 3000 km in both the zonal ( $X$ ) and meridional ( $Y$ ) directions, with a grid resolution of 5 km (Fig. 1a). There are 43 vertical levels with the interval varying from 10 m near the ocean surface

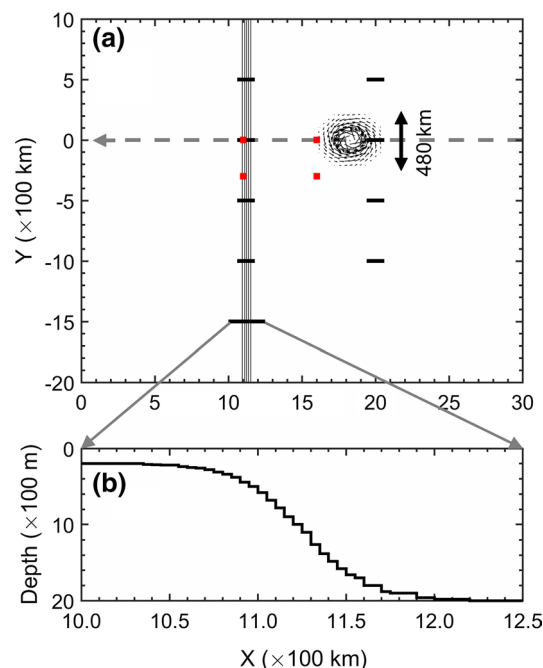


**Fig. 1** **a** The model domain. The water depth increases from 200 to 2000 m eastward. The gray solid lines running north–south indicate the isobaths (every 400 m from 400 to 2000 m). The frequency analysis in Fig. 2 is carried out along the eight short black solid lines. The four red squares denote the positions where vorticity diagnostics in Fig. 6 is carried out. The gray dashed arrow denotes the track of the typhoon traveling westward perpendicular to the shelf slope. A snapshot of the wind stress field with a radius of 240 km is superimposed on the track. **b** A zoomed cross-sectional view of the sloping bottom topography

to 100 m at the bottom. The bottom topography only varies in the zonal direction with a shallow region (200 m in depth) westward and a deep region (2000 m in depth) eastward, connected by a slope centered at  $x = 1125$  km (Fig. 1b). The gradient of the model shelf slope (0.02) is set to be close to the typical value of the ECS shelf slope.

In this study, we employ the  $\beta$ -plane approximation with the Coriolis parameter  $f = 3.1 \times 10^{-5} \text{ s}^{-1}$  at the south boundary of the domain and  $\beta = 2.1 \times 10^{-11} \text{ m}^{-1} \text{ s}^{-1}$ . The vertical viscosity and diffusivity are calculated using the K-profile parameterization scheme (Large et al. 1994). The background vertical viscosity ( $A_z$ ) and diffusivity ( $K_z$ ) are assumed to be  $10^{-4} \text{ m}^2 \text{ s}^{-1}$  and  $10^{-5} \text{ m}^2 \text{ s}^{-1}$ , respectively, whereas the background horizontal viscosity ( $A_H$ ) and diffusivity ( $K_H$ ) are assumed to be  $10^2 \text{ m}^2 \text{ s}^{-1}$  and  $10 \text{ m}^2 \text{ s}^{-1}$ , respectively. A no-slip boundary condition is employed, and the bottom stress is parameterized using the quadratic law with a constant drag coefficient  $C_d = 2.5 \times 10^{-3}$ .

The model is initialized with a horizontally homogeneous and vertically stratified temperature field. We first obtain the profiles of temperature and salinity by horizontally averaging the summer and autumn mean data obtained from

the World Ocean Atlas 2013 in the ECS shelf slope region (118–128°E, 22–28°N). The transport equation of salinity is closed in the model, but the employed temperature field is derived from the profiles of both temperature and salinity to reflect the effects of salinity on the stratification.

The model is initially at rest and forced with an idealized hurricane-type wind stress field that propagates westward with a constant speed. To prevent artificial wave reflections, sponge layers are assumed along the four open boundaries where the velocities are gradually decreased to zero toward the boundaries. The wind forcing is constructed following Price (1983), which has an axisymmetric wind stress field with a constant inflow angle of 17°. The maximum tangential wind stress is set to be 2.5 N m<sup>-2</sup>. In the control experiment, the typhoon has a radius of 240 km with a traveling speed of 5 m s<sup>-1</sup>. To investigate the response of TRWs to the change of typhoon parameters, we carry out a series of sensitivity experiments. The basic setting of the simulations remains the same as that in the control experiment, and only the radius and traveling speed of the typhoon are changed. The results of these sensitivity experiments are presented in Sect. 5.

### 3 Model results

The depth-averaged power spectra of current velocity in the frequency domain are first examined (Fig. 2). They show marked peaks at the inertial frequency ( $f_0$ , the inertial frequency at the latitude of the typhoon track) and its harmonics ( $2f_0$  and  $3f_0$ ) both over the flat and shelf slope regions. The spectral peaks at the inertial harmonics are in agreement with the numerical results of Niwa and Hibiya (1997), suggesting that these are induced by nonlinear interactions between high-vertical-mode NIWs. In addition to the inertial and inertial harmonic waves, there are two distinct subinertial peaks at  $\omega \approx 0.2f_0$  and  $0.8f_0$  found only over the shelf slope region (Fig. 2b). For simplicity, we hereafter call these two subinertial waves subf1 ( $0.8f_0$ ) and subf2 ( $0.2f_0$ ), respectively.

Figure 3 shows the time evolution of the bandpassed velocity along the shelf slope. Both subf1 and subf2 propagate southward with the shallow water on their right. As denoted by the black arrows in Fig. 3c, d, the phase speeds of subf1 and subf2 are estimated to be 4.9 and 1.8 m s<sup>-1</sup>, respectively. To further interpret the subinertial response over the shelf slope, we employ a linearized model for a continuously stratified Boussinesq ocean with the same shelf slope as used in the simulation. Although this model was originally derived to study the coastal trapped waves (Wang and Mooers 1976; Brink 1982), it is also applicable to the waves generated over the continental shelf slopes. In terms

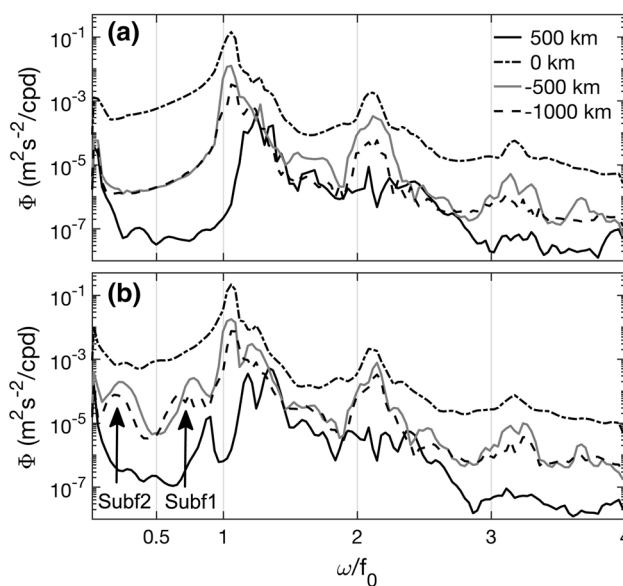


**Fig. 2** Depth-averaged power spectra of the numerically obtained current velocity in the **a** flat and **b** shelf slope regions. Different lines in each panel represent the results along the four zonal sections shown in Fig. 1.  $f_0$  is the inertial frequency at the latitude of the typhoon track. Two black arrows denote the two subinertial frequency peaks

of the pressure perturbation,  $P \sim e^{i(\omega t + ly)}$ , the governing equation for the waves can be written as

$$\frac{\partial^2 P}{\partial x^2} - l^2 P + (f^2 - \omega^2) \frac{\partial}{\partial z} \left( \frac{1}{N^2} \frac{\partial P}{\partial z} \right) = 0 \tag{1}$$

where  $l$  is the wavenumber in the  $y$  direction,  $f$  is the Coriolis frequency, and  $N^2$  is the squared buoyancy frequency. The boundary conditions for the trapped waves consist of (1) free surface boundary, (2) no flow through the solid bottom, (3) no disturbances far offshore, and (4) no normal flow at the coast. The governing equation (Eq. 1) together with these boundary conditions form a two-dimensional eigenvalue problem. In solving this eigenvalue problem, we exploited the code presented by Brink (2006; see also <http://www.whoi.edu/page.do?pid=23361>).

The existence of the first two-mode TRWs, at least, can be recognized as the subinertial frequency spectral peaks on the dispersion curves at nearly the same along-slope wavenumber of  $\sim 2 \times 10^{-6}$  cpm (Fig. 4). Figure 5c, d shows the numerically obtained along-slope velocity fields at 500 km southward from the typhoon track associated with subf1 and subf2, respectively, which are confined near the sloping bottom due to the presence of stratification (Wang and Mooers 1976; Tanaka et al. 2010) and correspond very well to the theoretical cross-slope structures of mode 1 and mode 2 TRWs shown in Fig. 5a, b, respectively. Putting all the obtained results together, we can conclude that these

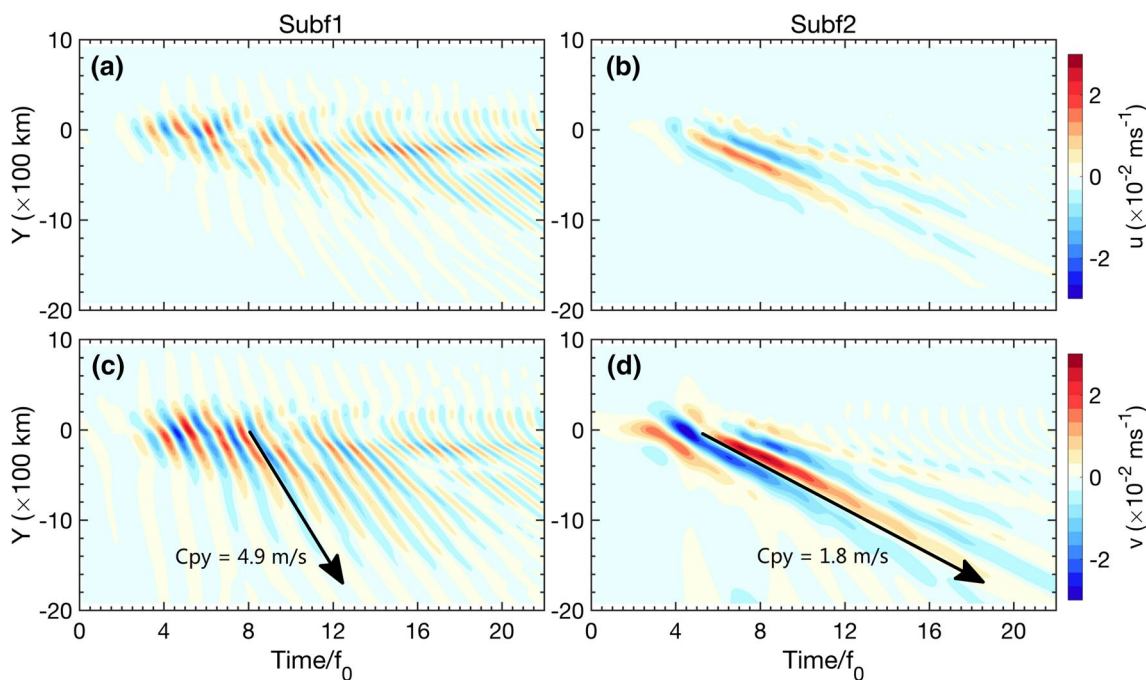


**Fig. 3** Time variations of the numerically obtained zonal (a, b) and meridional (c, d) velocity components at the bottom along  $X=1150$  km. The water depth is 1550 m. The velocities of subf1 (a,

c) and subf2 (b, d) are bandpassed  $0.55-0.9f_0$  and  $0.05-0.5f_0$ , respectively. The black arrows denote the phase propagation

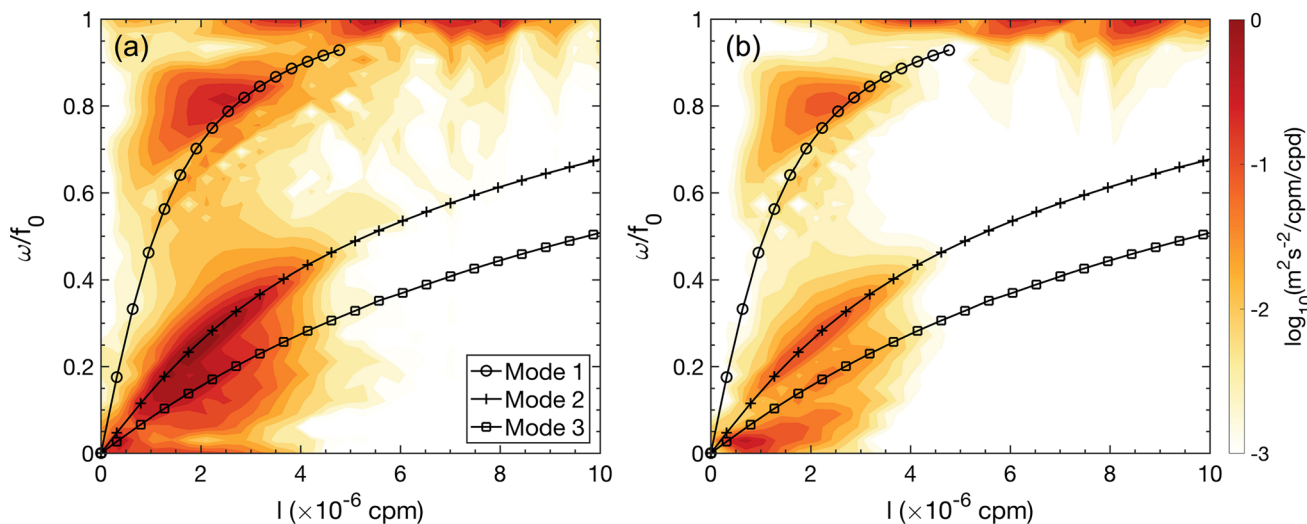


**Fig. 4** Meridional (along-slope) wavenumber–frequency spectra of the numerically obtained horizontal kinetic energy near the bottom along **a**  $X=1100$  km and **b**  $X=1150$  km. Note that these are created by calculating the meridional wavenumber spectrum for each frequency band horizontal kinetic energy. The three lines represent the

theoretical dispersion curves of the first three mode TRWs obtained by solving the eigenvalue problem (Eq. 1). Here,  $l>0$  represents the southward propagation. The other half of spectra with  $l<0$  are not shown because of their negligible values

subinertial motions generated by the traveling typhoon are associated with the mode 1 and mode 2 TRWs propagating along the shelf slope.

## 4 Discussion

### 4.1 Vorticity balance

The generation mechanism of TRWs can be explained in terms of the conservation of potential vorticity ( $\frac{f+\zeta}{H}$ ) over the sloping

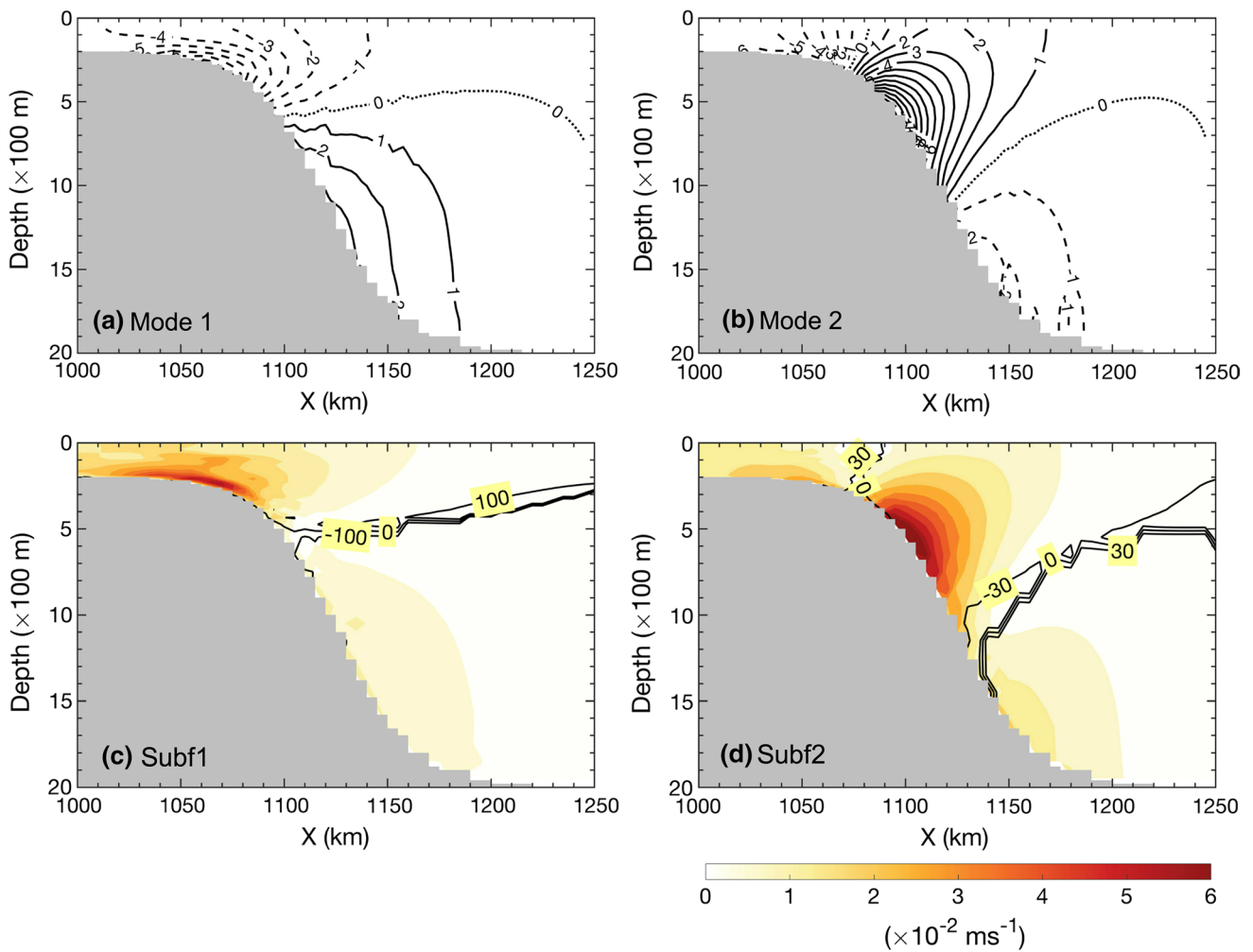


**Fig. 5** Upper panels cross-slope distribution of the theoretically predicted along-slope velocity associated with **a** mode 1 and **b** mode 2 TRW. The frequencies are set to be  $0.8f_0$  and  $0.2f_0$  in solving the eigenvalue problem for mode 1 and mode 2 TRWs, respectively. The contour units are arbitrary. Lower panels cross-slope distribu-

tion of the amplitude (color) and phase (contours) of the numerically obtained along-slope velocity along  $Y = -500$  km associated with **c** subf1 and **d** subf2, which are bandpassed  $0.55-0.9f_0$  and  $0.05-0.5f_0$ , respectively

bottom (Gill 1982). When the continental shelf slope is steep enough to dominate the potential vorticity balance, the cross-isobath motions cause the stretching or shrinking of the water column, creating the cyclonic or anti-cyclonic motion. To quantitatively examine the role of each term in the generation and propagation of the TRW, the depth-integrated vorticity balance is diagnosed. By depth-integrating the momentum equations and then taking the curl of them, we can derive the depth-integrated vorticity equation as

$$\begin{aligned}
 & \frac{\partial \zeta}{\partial t} - \frac{\partial \eta}{\partial t} \text{curl}(u, v)|_{\eta} \\
 &= -\beta V + \frac{1}{\rho_0} J(p_b, H) - \text{curl} \left[ \int_{-H}^{\eta} (\mathcal{A}(u), \mathcal{A}(v)) dz \right] \\
 &+ \text{curl} \left[ \int_{-H}^{\eta} (\mathcal{V}_h(u), \mathcal{V}_h(v)) dz \right] + \text{curl} \frac{\boldsymbol{\tau}_s}{\rho_0} - \text{curl} \frac{\boldsymbol{\tau}_b}{\rho_0}
 \end{aligned} \tag{2}$$

where two operators are defined as  $J(A, B) = \frac{\partial A}{\partial x} \frac{\partial B}{\partial y} - \frac{\partial A}{\partial y} \frac{\partial B}{\partial x}$  and  $\text{curl}(\mathbf{C}) = \frac{\partial C_y}{\partial x} - \frac{\partial C_x}{\partial y}$ ,  $u$  and  $v$  are the calculated eastward and northward velocities, respectively,  $\zeta = \frac{\partial V}{\partial x} - \frac{\partial U}{\partial y}$  is the vorticity of depth-integrated velocity  $U$  and  $V$ ,  $\eta$  is the sea surface height,  $H$  is the water depth,  $\rho_0$  is the reference water density,  $p_b$  is the bottom pressure, operators  $\mathcal{A}$  and  $\mathcal{V}_h$  denote the advection and the horizontal viscosity, respectively, and  $\boldsymbol{\tau}_s = (\tau_{sx}, \tau_{sy})$  and  $\boldsymbol{\tau}_b = (\tau_{bx}, \tau_{by})$  are the wind stress and the bottom stress, respectively. The terms on the right-hand side represent the beta effect, the bottom pressure torque, the curl of the horizontal momentum advection, the curl of the horizontal viscosity, and the curl of the wind and bottom stresses. The bottom pressure torque term is induced by the pressure difference along the isobaths and is the only term related to the bottom topography (Mertz and Wright 1992).

The ratio of the second to the first term on the left-hand side is very small ( $\sim \frac{\Delta\eta}{H}$ ), so that the tendency of the depth-integrated vorticity ( $\frac{\partial\zeta}{\partial t}$ ) is balanced by the six terms on the right-hand side.

Figure 6 shows the time series of the diagnosed vorticity balance. In the flat region, subinertial motions are generated under the typhoon track, and the balance is mainly between the wind stress ( $\text{curl}\frac{\tau_s}{\rho_0}$ ) and subinertial tendency ( $\frac{\partial\zeta}{\partial t}$ ) (Fig. 6a). However, no corresponding subinertial signal can be detected 300 km southward from the typhoon track, namely, out of the typhoon radius (Fig. 6d). This means that the subinertial wave generated under the typhoon track in the flat region is a kind of forced wave and cannot freely propagate out of the direct effect of the typhoon.

As the typhoon approaches the shelf slope region, the bottom pressure torque comes into balance (Fig. 6b, c). Under the typhoon track, the dominant vorticity balance becomes mainly among the subinertial tendency, the wind stress, and the bottom pressure torque. The subinertial wave can freely propagate out of the wind forcing region (Fig. 6e, f) where

the subinertial tendency is primarily balanced by the bottom pressure torque.

The above analysis shows that the bottom pressure torque ( $\frac{1}{\rho_0}J(p_b, H)$ ) plays a crucial role in both the generation and propagation of TRWs. In the presence of sloping topography, the pressure force from the topography into the ocean has a horizontal component. When this horizontal component changes along the isobaths, the difference can create the “twisting force” on the overlying fluid (Jackson et al. 2006). For the question discussed here, disturbances induced by the approaching typhoon is the original reason that causes the change of the density field and then the bottom pressure field along the isobaths.

### 4.2 The sensitivity of TRW properties to typhoon parameters

In this section, we demonstrate how the TRW response (i.e., the frequency/along-slope wavenumber and intensity) is controlled by the typhoon parameters (radius and traveling

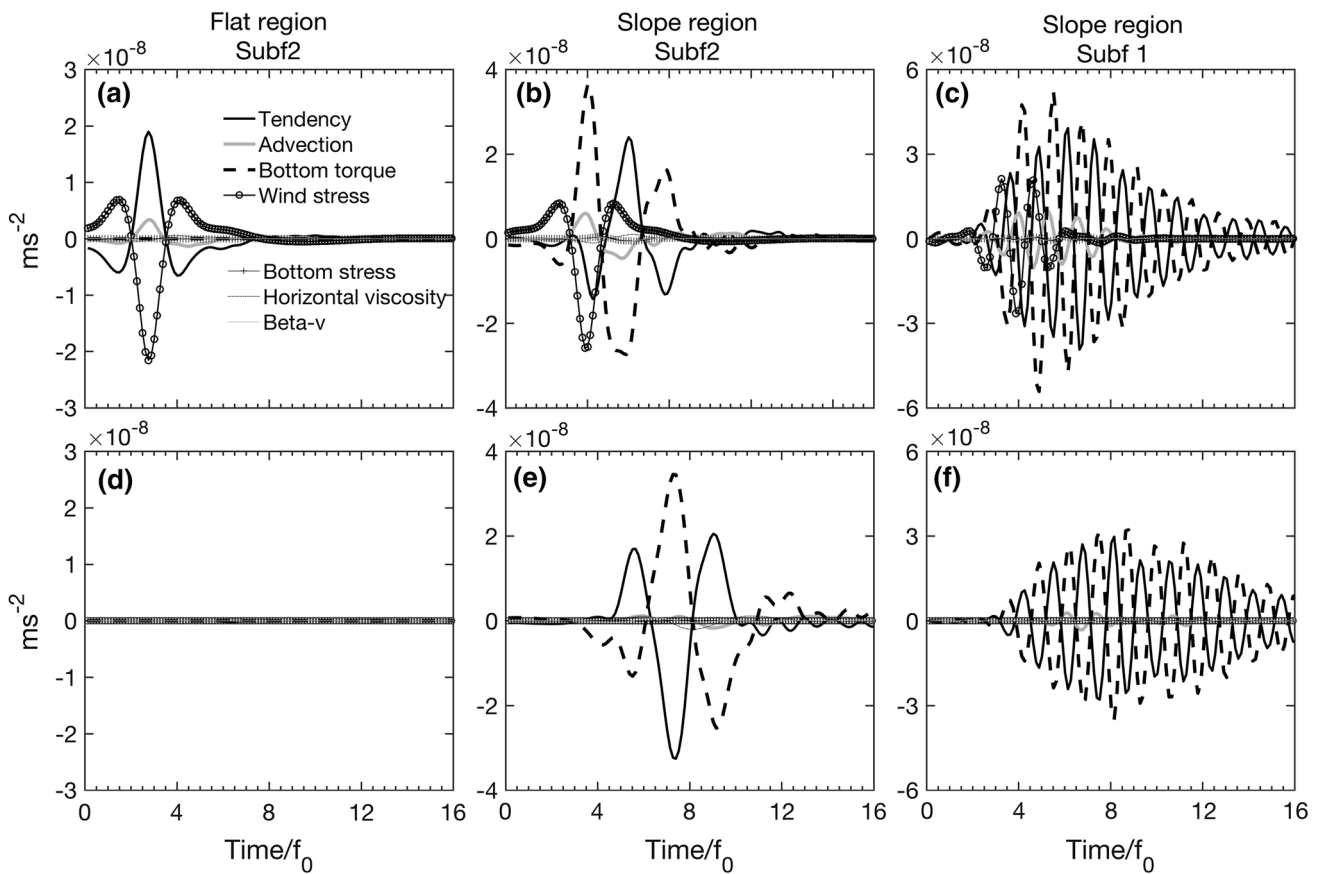


**Fig. 6** Time series of each term in the depth-integrated vorticity equation (Eq. 2). **a, b, d, e** are for subf2 ( $0.05\text{--}0.5f_0$ ) and **c** and **f** are for subf1 ( $0.55\text{--}0.9f_0$ ) averaged within a small square area in the flat region (**a**  $1600 < X < 1610$  km,  $-5 < Y < 5$  km; **d**  $1600 < X < 1610$  km,

$-305 < Y < -295$  km) or the slope region (**b, c**  $1100 < X < 1110$  km,  $-5 < Y < 5$  km; **e, f**  $1100 < X < 1110$  km,  $-305 < Y < -295$  km). The corresponding locations are also shown in Fig. 1

speed) by carrying out two sets of sensitivity experiments. In the first set, the typhoon traveling speed remains unchanged ( $5 \text{ m s}^{-1}$ ) but the typhoon radius is gradually increased from 90 to 720 km. In the second set, the typhoon radius is fixed (240 km) but the typhoon traveling speed is increased or decreased by a factor of two. The basic numerical setting (e.g., bottom topography and stratification) in the sensitivity experiments is otherwise the same as that in the control experiment.

Figure 7a and b show the along-slope wavenumber and frequency spectra calculated using the results from the first set of sensitivity experiments. The along-slope wavenumber spectra are obtained by averaging the wavenumber–frequency spectra over the frequency range between  $0.05f_0$  and  $0.95f_0$ . One robust result of the wavenumber spectra is that the wavenumber of the energy peak decreases with the increase of the typhoon radius (Fig. 7a); the along-slope wavelength ( $\lambda = \frac{1}{l}$ ) has a positive correlation with the typhoon radius ( $R$ ), and the best linear fitting between them is  $\lambda = R + 230 \text{ km}$  with the correlation coefficient 0.92.

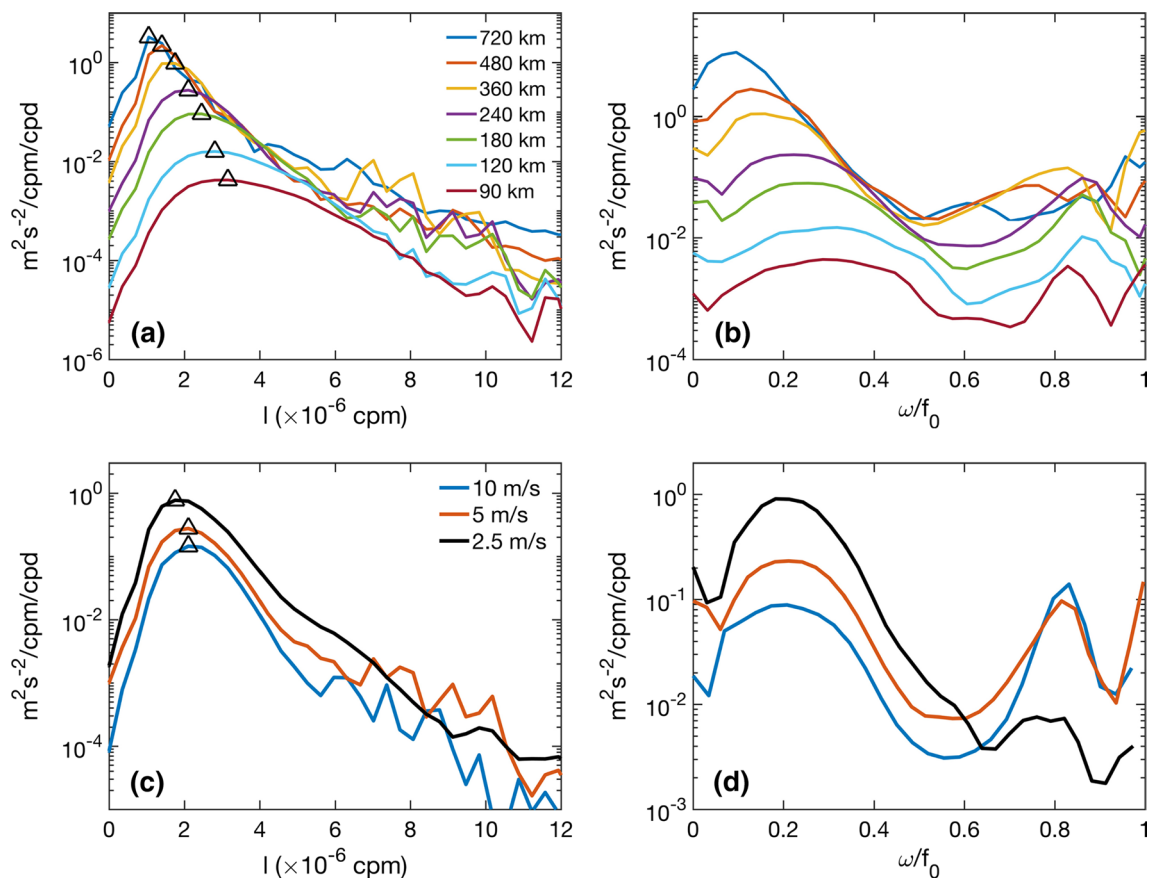


**Fig. 7** The along-slope wavenumber spectra obtained by averaging the wavenumber–frequency spectra over the frequency range between  $0.05$  and  $0.95f_0$  (**a**, **c**) with the corresponding frequency spectra obtained by averaging over the wavenumber range between  $0$  and  $10^{-5} \text{ cpm}$  (**b**, **d**). Note that the typhoon traveling speed remains

The frequency of the energy peak is also correlated with the typhoon radius through the TRW dispersion relationship (Fig. 7b).

Next, the results of the second set of sensitivity experiments are examined. Unlike the first set of sensitivity experiments, the along-slope wavenumber of the spectral peak remains constant at  $\sim 2 \times 10^{-6} \text{ cpm}$  with two subinertial frequency peaks fixed at  $0.2f_0$  and  $0.8f_0$  (Fig. 7c, d). These results indicate that it is not the traveling speed but the radius of the typhoon which has a “decisive” effect on the resulting TRW properties, such as the along-slope wavenumber and frequency. This is a new finding because previous studies have never focused on the relationship in the spatial scale between the large-scale wind forcing and subinertial ocean currents (e.g., Brooks and Mooers 1977; Miller et al. 1996; Wahlin et al. 2016).

The vertical structures of the generated TRWs, on the other hand, depend on both the typhoon radius and the typhoon traveling speed (Fig. 7c, d). Although the mode 2 TRW is generally more energetic than the mode 1 TRW,

at  $5 \text{ m s}^{-1}$  and the typhoon radius is gradually increased from 90 to 720 km in **a** and **b**, while the typhoon radius is fixed at 240 km and the typhoon traveling speed is increased from 2.5 to  $10 \text{ m s}^{-1}$  in **c** and **d**. Each black triangle in **a** and **c** denotes the position of the maximum value

the latter amplifies as the typhoon traveling speed increases or the typhoon radius decreases. It must be noted, however, that, in this study, the dependence of the frequency and wavenumber of the generated TRWs on the typhoon radius and the typhoon traveling speed is addressed for a special case in which a typhoon travels perpendicular to the shelf slope. Changing the propagation direction of the typhoon may induce more complicated stratified ocean responses, which remain to be examined in the future.

### 4.3 Predominance of NIW or TRW

The NIWs are usually thought to be the most dominant oceanic response to traveling typhoons (e.g., Gill 1984). However, recent studies have begun to find that there may also exist strong subinertial motions as a response to storms passing over the oceanic topographic slopes or ridges (Dukhovskoy et al. 2009; Igeta et al. 2011). To quantitatively compare the energetics between TRWs and NIWs, we calculate the vertically integrated meridional energy fluxes given by

$$F_y = \int_{-H}^0 p'v' dz \quad (3)$$

where the prime (') represents the bandpass-filtered variables for the corresponding frequency range.  $p'$  and  $v'$  are thus the hydrostatic pressure perturbation and meridional velocity filtered in frequency domain, respectively, and  $z = -H$  is the ocean bottom. Once the energy flux is integrated across a zonal section over the continental shelf slope, the cumulative integral with time can be calculated as

$$KE = \int_0^t \int_{1000 \text{ km}}^{1250 \text{ km}} F_y dx dt \quad (4)$$

where  $X = 1000$  and  $1250$  km represent the west and east boundary of the zonal section (corresponding to the shelf slope region), respectively. Equation 4 thus represents the typhoon-generated wave energy propagating in the meridional direction across the zonal section over the shelf slope.

Figure 8 shows an example of the time-cumulated integral of energy flux. The results of different sensitivity experiments are summarized in Fig. 9. As discussed in Sect. 4.2, the typhoon radius and traveling speed both control the amplitude of TRWs. Figure 9 shows that the subinertial energy can be comparable to or more than the near-inertial energy for typhoons with large radii (480 and 720 km) or a slow traveling speed ( $2.5 \text{ m s}^{-1}$ ). This indicates that, under these particular conditions, TRWs can carry more energy along the shelf slope than NIWs.

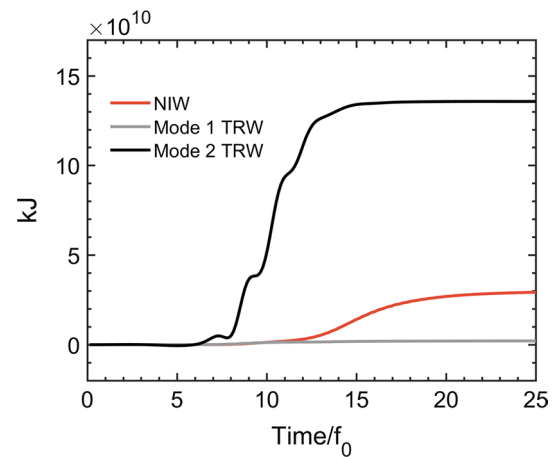


**Fig. 8** The cumulative integral of energy flux with time through the zonal section between  $X = 1000$  and  $1250$  km along  $Y = -240$  km (240 km southward from the typhoon track) (Eq. 4). The typhoon has a radius of 240 km and a traveling speed of  $2.5 \text{ m s}^{-1}$ . This zonal section thus locates at the southern edge of the typhoon. The results for the NIW, and mode 1 and mode 2 TRWs are calculated from the hydrostatic pressure perturbation and velocity bandpassed  $0.95-1.3f_0$ ,  $0.55-0.9f_0$ , and  $0.05-0.5f_0$ , respectively. Note that the negative sign in the cumulated energy flux is omitted here

The generated wave energy is closely related to the predominant frequency of the wind stress field. In this linear system, more energy is injected into the waves with the frequencies close to those of the predominant wind stress field. This induces the energy peaks of the NIW and mode 1 TRW at the typhoon radii of 240 and 360 km (Fig. 9a), respectively. Since the TRWs are bottom-intensified, they may directly change the near-bottom mixing along their path. More realistic numerical simulations are needed to document the dissipation processes of the typhoon-generated TRWs as well as their effects on the water-mass deformation and the circulation system in the ECS.

## 5 Conclusions

This study has focused on the subinertial waves excited by a typhoon traveling over the ocean with a continental shelf slope. The idealized numerical simulations with a simplified sloping topography and stratification typical of the East China Sea have demonstrated that, in addition to the inertial waves and their inertial harmonics, subinertial waves have been excited with their energy peaks at  $\omega = 0.2f_0$  and  $0.8f_0$ . These subinertial waves follow the theoretical dispersion curves of the TRWs, and at least the first two modes can be clearly identified to be bottom-trapped with their amplitudes increasing toward the seabed. The main conclusions are as follows:



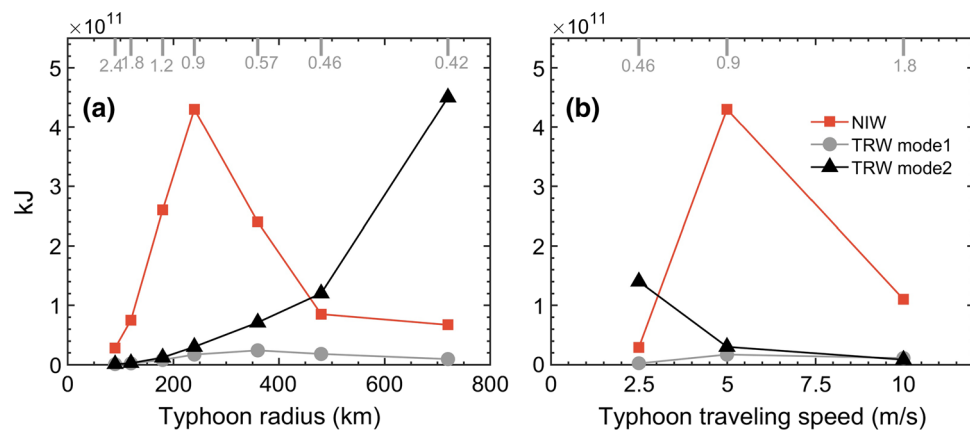


**Fig. 9** The time-cumulated zonally-integrated energy fluxes that pass the zonal sections at the southern edges of typhoons ( $Y = -R$ ) until  $25f_0$  (Eq. 4). The typhoon traveling speed remains at  $5 \text{ m s}^{-1}$  and the typhoon radius is gradually increased from 90 to 270 km in **a**, whereas the typhoon radius is fixed at 240 km and the typhoon travel-

ing speed is increased from 2.5 to  $10 \text{ m s}^{-1}$  in **b**. The corresponding predominant frequencies of different wind stress fields ( $\omega/\omega_f$ ) are shown on the *top axes*. Note that all the negative signs in the cumulated energy fluxes are omitted here

1. The diagnostics of the depth-integrated vorticity balance associated with the TRWs show that the subinertial tendencies are balanced by the wind stress and the bottom pressure torque in the wind forcing region over the shelf slope, and are primarily balanced by the bottom pressure torque out of the wind forcing region. The vorticity analysis thus demonstrates the importance of the bottom pressure torque in both the generation and propagation processes of TRWs. In contrast, in the flat region, although subinertial motions are also generated immediately below the typhoon track, they remain as forced waves and no subinertial signal can be detected out of the typhoon track.
2. Two sets of sensitivity experiments show that the typhoon radius is a “decisive” parameter in determining the frequency and wavenumber of the generated TRWs; the along-slope wavenumber of the generated TRWs is first determined by the typhoon radius, and the frequency is next determined so as to satisfy the dispersion relationship.
3. The vertical structures of the generated TRWs (such as which of the mode 1 and 2 TRWs becomes dominant) are determined by both the typhoon radius and the typhoon traveling speed. Furthermore, energetics analysis shows that for a typhoon with a large radius or slow traveling speed, the subinertial TRW can transport comparable or more energy southward than the near-inertial waves. This indicates that the TRWs might play an important role in inducing the near-bottom mixing along the shelf slope by using energy supplied from typhoon winds.

**Acknowledgements** The initial buoyancy field were obtained from the World Ocean Atlas (<https://www.nodc.noaa.gov/OC5/woa13/>). The model results supporting this paper are publicly available at <https://figshare.com/s/6b56e8f8ed33dfea0830>. This study was supported by the National Key Research and Development Program of China (Grant No. 2016YFA0601301). L. Zhao thanks the support from the National Natural Science Foundation of China (NSFC, 41876018). H. Wei thanks the support from the National Key Research and Development Program of China (Grant Nos. 2016YFC1401401 and 2017YFC1404403).

## References

- Brink KH (1982) A comparison of long coastal-trapped wave theory with observations off Peru. *J Phys Oceanogr* 12:897–913
- Brink KH (2006) Coastal-trapped waves with finite bottom friction. *Dyn Atmos Oceans* 41:172–190
- Brooks DA, Mooers CNK (1977) Wind-forced continental shelf waves in the Florida current. *J Geophys Res* 82:2576–2669
- Damerell G, Heywood KJ, Stevens DP, Naverira Garabato AC (2012) Temporal variability of diapycnal mixing in Shag Rocks Passage. *J Phys Oceanogr* 42:370–385. <https://doi.org/10.1175/2011JPO4573.1>
- Dukhovskoy DS, Morey SL, O’Brien JJ (2009) Generation of baroclinic topographic waves by a tropical cyclone impacting a low-latitude continental shelf. *Cont Shelf Res* 29:333–351
- Emanuel KA (2005) *Divine wind, the history and science of hurricanes*. Oxford University Press, New York
- Furuichi N, Hibiya T, Niwa Y (2008) Model-predicted distribution of wind-induced internal wave energy in the world’s oceans. *J Geophys Res Oceans* 113:C09034. <https://doi.org/10.1029/2008JC004768>
- Gill AE (1982) *Atmosphere-ocean dynamics*. Academic, New York
- Gill AE (1984) On the behavior of internal waves in the wake of storms. *J Phys Oceanogr* 14:1129–1151
- Igeta Y, Watanabe T, Yamada H, Takayama K, Katoh O (2011) Coastal currents caused by superposition of coastal-trapped waves and

- near-inertial oscillations observed near the Noto Peninsula, Japan. *Cont Shelf Res* 31:1739–1749
- Jackson L, Hughes CW, Williams RG (2006) Topographic control of basin and channel flows: The role of bottom pressure torques and friction. *J Phys Oceanogr* 36:1786–1805
- Jensen MF, Fer I, Darelius E (2013) Low frequency variability on the continental slope of the southern Weddell Sea. *J Geophys Res Oceans* 118:4256–4272. <https://doi.org/10.1002/jgrc.20309>
- Large WG, McWilliams JC, Doney SC (1994) Oceanic vertical mixing: a review and a model with a nonlocal boundary layer parameterization. *Rev Geophys* 32:363–403
- Mertz G, Wright DG (1992) Interpretations of the JEBAR term. *J Phys Oceanogr* 22(3):301–305
- Miller AJ, Lermusiaux PFJ, Poulain PM (1996) A topographic Rossby-mode resonance over the Iceland-Faeroe Ridge. *J Phys Oceanogr* 26:2735–2747. [https://doi.org/10.1175/1520-0485\(1996\)026,2735:ATMROT.2.0.CO;2](https://doi.org/10.1175/1520-0485(1996)026<2735:ATMROT.2.0.CO;2)
- Niwa Y, Hibiya T (1997) Nonlinear processes of energy transfer from traveling hurricanes to the deep ocean internal wave field. *J Geophys Res* 102(C6):12469–12477. <https://doi.org/10.1029/97JC00588>
- Oey LY, Lee HC (2002) Deep eddy energy and topographic Rossby waves in the Gulf of Mexico. *J Phys Oceanogr* 32:3499–3527
- Pickart RS (1995) Gulf stream-generated topographic Rossby waves. *J Phys Oceanogr* 25:574–586
- Price JF (1983) Internal wave wake of a moving storm. Part I: scales, energy budget and observations. *J Phys Oceanogr* 13:949–965
- Rivas D (2017) Wind-driven coastal-trapped waves off southern Tamaulipas and northern Veracruz, western Gulf of Mexico, during winter 2012–2013. *Estuar Coast Shelf S* 185:1–10
- Tada H, Uchiyama Y, Masunaga E (2018) Impacts of two super typhoons on the Kuroshio and marginal seas on the Pacific coast of Japan. *Deep Sea Res Part I* 32:80–93
- Tanaka Y, Hibiya T, Niwa Y, Iwamae N (2010) Numerical study of  $K_1$  internal tides in the Kuril Straits. *J Geophys Res* 115:C09016. <https://doi.org/10.1029/2009JC005903>
- Teague WJ, Jarosz E, Wang DW, Mitchell DA (2007) Observed oceanic response over the upper continental slope and outer shelf during Hurricane Ivan. *J Phys Oceanogr* 37:2181–2206
- Thompson RORY, Luyten JR (1976) Evidence for bottom trapped topographic Rossby waves from single moorings. *Deep-Sea Res* 23:629–635
- Wahlin AK, Kalen O, Assmann KM, Darelius E, Ha HK, Kim TW, Lee SH (2016) Subinertial oscillations on the Amundsen Sea Shelf, Antarctica. *J Phys Oceanogr* 46:2573–2582
- Wang DP, Mooers CNK (1976) Coastal-trapped waves in a continuously stratified ocean. *J Phys Oceanogr* 6:853–863
- Wang ZK, DiMarco SF, Stössel MM, Zhang X, Howard MK, Vall K (2012) Oscillation responses to tropical Cyclone Gonu in northern Arabian Sea from a moored observing system. *Deep Sea Res Part I* 64:129–145